APPLIED SCIENCES AND ENGINEERING

Bio-inspired organic electrosense transistor for impalpable perception

Cong Wang[1]†, Jiaofu Li[1]†, Xufan Li[2]†, Wenlong Li[3], Yanzhen Li[1], Yinan Huang[4], Changxian Wang[1], Zhihua Liu[3], Ming Wang[1], Nuan Chen[1], Mingxi Chen[3], Liang Pan[1], Feilong Zhang[1]‡, Jinshun Bi[2], Liqiang Li[4], Wenping Hu[4]*, Xiaodong Chen[1]*

Artificial sense technologies predominantly rely on visual and tactile input, which often prove inadequate in obscured or opaque environments. Inspired by the natural electrosensory capabilities of electrogenic fishes, we introduce an organic electrosense transistor designed to detect electric fields generated by nearby objects, facilitating the creation of impalpable perception systems. Unlike traditional sensors, our electrosense transistor perceives bipolar electric fields with high sensitivity and stability. We use compact models and device simulations to elucidate the mechanisms of charge induction and transport within organic electrosense transistors when exposed to spatial electric fields. Demonstrating its practical utility, we show that robots equipped with our electrosense transistor can successfully navigate and detect concealed objects without requiring direct contact. This work not only advances the understanding of charge dynamics in electrosensory systems but also establishes a platform for developing highly sensitive, noninvasive artificial sensing technologies applicable in surveillance, search and rescue, and other challenging environments.

INTRODUCTION

By mimicking human visual and tactile perception, artificial sense technologies are making remarkable strides, enhancing our interactions with humanoid robots (*1*–*4*), prosthetic devices (*5*–*8*), and virtual/augmented reality experiences (*9*–*11*). However, they work either under well-controlled lighting or within touchable conditions. For hidden objects or unstable ambient light, impalpable sense technologies are expected to fill in the gap. Infrared (*12*) or ultrasound (*13*) impalpable detection relies on reflecting photonic or acoustic signals, limiting detection to objects within a specific direction. Magnetism (*14*, *15*) or humidity (*16*, *17*) has also been explored for contactless detection, but their sensing range is limited to 1 cm. Some animals, such as elasmobranch fishes and monotremes, have a "sixth sense." They use electroreceptive cells to detect electrical fields in their surroundings, allowing them to navigate and hunt in low-visibility conditions, like dark ocean or muddy riverbeds (*18*). This provides an inspiring approach to developing electrosense devices sustaining perception even when visual and tactile senses are not feasible.

Although electrosense devices based on conductors and semiconductors have been developed for the detection of charged objects, they are not as exquisite as their biological counterparts, especially in terms of sensitivity, polarity differentiation, and on-demand output. For example, capacitive devices based on conducting materials could be configured to detect a moving charged object (*19*–*24*). The device operates via electrostatic induction and charge transfer, producing current or voltage signals when charged objects approach or depart. However, it is incapable of perceiving slow-moving or stationary objects, distinguishing charge polarity, and determining the direction of movement. Field-effect transistors based on semiconductors, in theory, are promising artificial receptors for spatial electric fields because the resistance of the channel can be modulated by several orders of magnitudes. However, it remains a critical challenge to achieve high sensitivity and stability due to the insufficient understanding of charge dynamics (involving charge induction and charge transport) and the lack of quantitative models to guide device design (*25*–*28*). Moreover, current electrosense devices do not demonstrate sensitivity to electric field strength. Addressing these challenges is crucial to designing electrosense devices on-demand and advancing the development of impalpable sense technologies.

Here, we show how an organic electrosense transistor (denoted as EST) mimics the functionality of electroreceptive cells and reveal the charge dynamics to implement a highly sensitive, polar-identifying impalpable electro-sensing device. Modeled on voltage-gated ion channels to regulate the transmembrane conductance of electroreceptive cells (Fig. 1, A and B), our EST has organic semiconductor crystal films (OSCFs) as a spatial electric field-gated carrier channel and a conductive charge-pumping layer (CPL) separated by a dielectric (Fig. 1, C to F, and fig. S1). By establishing a compact model, conducting simulations, and performing experimental verification, we found that the CPL, acting as a charge reservoir, enhances charge induction in the channel through the charge-pumping effect. Then, we theoretically predicted the programmable time-dependent response and experimentally verified it by controlling the crystallinity of the semiconductor channel. As a result, the EST based on OSFCs shows a detection limit of -0.12 kV m^{-1} for negative stimuli and 0.61 kV m^{-1} for positive stimuli, respectively. Our EST can differentiate electrostatic polarity and effectively detect slow-moving objects with steady response. Crawling robots implemented with EST can

[1]Innovative Center for Flexible Devices (iFLEX), Max Planck – NTU Joint Lab for Artificial Senses, School of Materials Science and Engineering, Nanyang Technological University, 50 Nanyang Avenue, 639798 Singapore, Singapore. [2]State Key Lab of Fabrication Technologies for Integrated Circuits, Institute of Microelectronics, Chinese Academy of Sciences, Beijing 100029, China. [3]Institute of Materials Research and Engineering (IMRE), Agency for Science, Technology and Research (A*STAR), 2 Fusionopolis Way, Innovis #08-03, 138634 Singapore, Singapore. [4]Key Laboratory of Organic Integrated Circuits of Ministry of Education, Tianjin Key Laboratory of Molecular Optoelectronic Sciences, Department of Chemistry, Institute of Molecular Aggregation Science, Tianjin University, Tianjin 300072, China.
*Corresponding author. Email: huwp@tju.edu.cn (W.H.); chenxd@ntu.edu.sg (X.C.)
†These authors contributed equally to this work.
‡Present address: CAS Key Laboratory of Bio-inspired Materials and Interfacial Science, Technical Institute of Physics and Chemistry, Chinese Academy of Sciences, Beijing 100190, China.

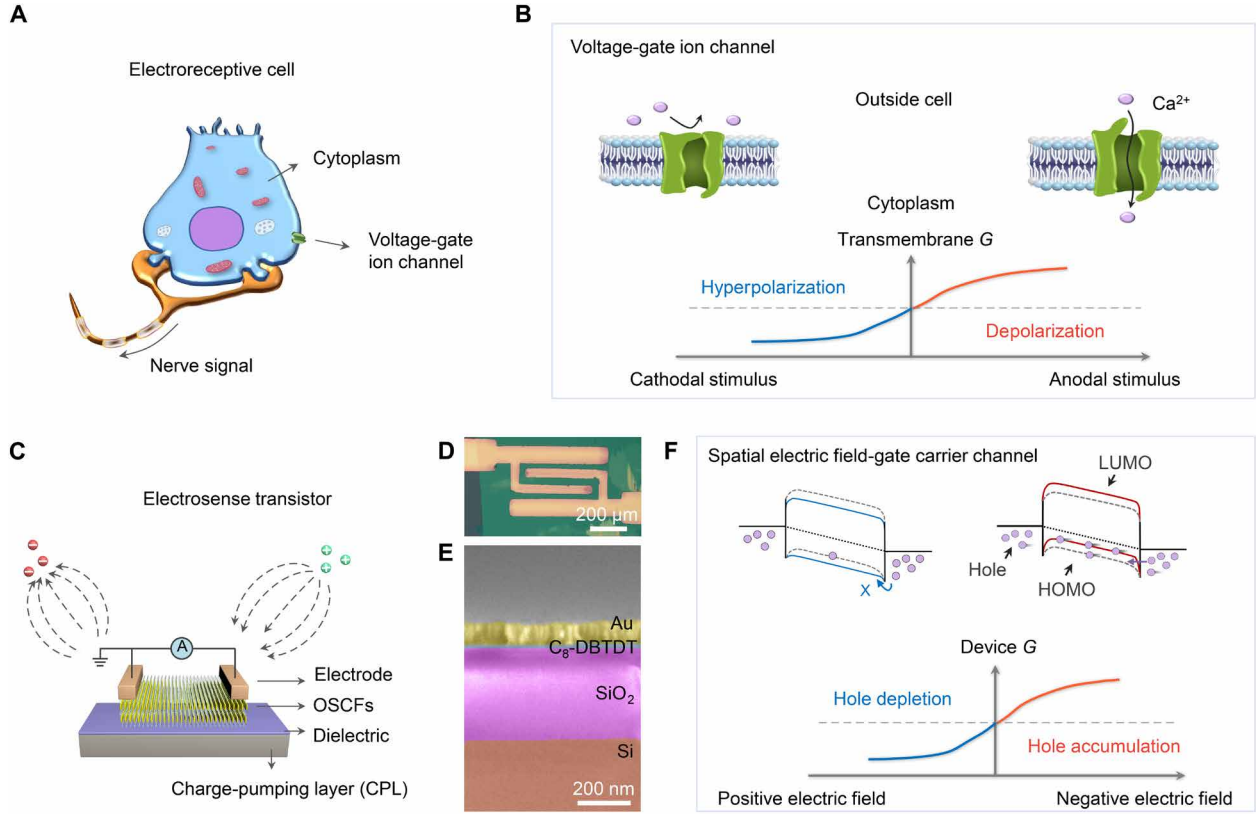

Fig. 1. Concept design of the EST inspired by the electroreceptive cell. (**A** and **B**) Conceptual graph (A) and sensing mechanism (B) of typical electrosensory cells. The hyperpolarization and depolarization of cell membranes caused by electric field stimulation generate nerve signals that enable impalpable perception. (**C** to **F**) Diagram (C), optical micrograph (D), and cross-sectional scanning electron microscope image (E) of our EST, whose carrier channel regulated by spatial electric field imitates the voltage-gate ion channels of electroreceptive cells, resulting in detectable electric signal (F). OSCFs, organic semiconductor crystal films. C_8-DBTDT, dioctyl-substituted dibenzo[d,d′]thieno[3,2-b;4,5-b′]-dithiophenes. HOMO, highest occupied molecular orbital; LUMO, lowest unoccupied molecular orbital. *G*, conductance.

rapidly respond to positively and negatively charged obstacles and detect hidden objects. Such an impalpable electrosensory system is useful for patrolling hazardous environments and operating intelligent search-and-rescue tasks.

RESULTS

Charge pumping enhances charge induction in EST

Our EST detects electric fields through two key steps: First, the spatial electric field induces charges in the semiconducting layer; second, the induced charges are transported within the semiconducting layer, and the resulting current is measured using two electrodes. To maximize charge induction, we used a conducting Si (p^+) (boron-doped silicon) as CPL covered by a dielectric layer (300-nm SiO_2) (Fig. 2A), which can notably generate more induced holes in the highest occupied molecular orbital (HOMO) of the semiconducting crystal due to charge-pumping effect. On the contrary, transistor-like electric field-sensing devices usually use an insulated substrate without a CPL (denoted as resistor; Fig. 2B), generating fewer carriers. To investigate how charge induction occurs in the EST, we developed a finite element analysis (FEA) model (Fig. 2C, text S1, and fig. S2). The device in the model maintains the same geometric proportions as the device in experiments (table S1). We used an indium tin oxide–coated glass slide, biased by a stepwise DC voltage ranging from 0 to −3.5 kV and 0 to +1.0 kV, to generate the bipolar spatial electric field. The device was positioned parallel to the stimulus at 10 mm.

The FEA simulation demonstrates that our EST enables the electric field lines (e.g., at $V_{sti} = -200$ V) to converge on the CPL, forming equipotential lines on the CPL and generating the induced potential ($\varphi_{induced}$) (Fig. 2C). The magnified potential distribution indicates that conductive CPL counteracts the internal potential drop due to effective charge separation. The simulated $\varphi_{induced}$ is −0.64 V relative to the potential of CPL in zero electric field stimulus (φ_0), which is consistent with the experimental results (fig. S3). On the contrary, the resistor device has an obvious potential drop in its insulated substrate (Fig. 2D). The simulated induced charges (σ_d) of the electrode/semiconductor interface grow with permittivity of CPL (ε_{CPL}) and approach infinitely to the value where CPL is the conductor (Fig. 2E). As a result, the σ_d of EST (1.8×10^{-4} C m^{-2}) is nearly 10 times than that of the resistor device (0.19×10^{-4} C m^{-2}). This is because the conductor CPL is considered to have an infinite permittivity that can provide large numbers of charges under the external electric field to move to the CPL/dielectric interface. Our modeling results suggest that using a conducting CPL, such as doped conductive silicon and other conducting materials, can effectively enhance induced charges through the charge-pumping effect. This charge-pumping effect is not

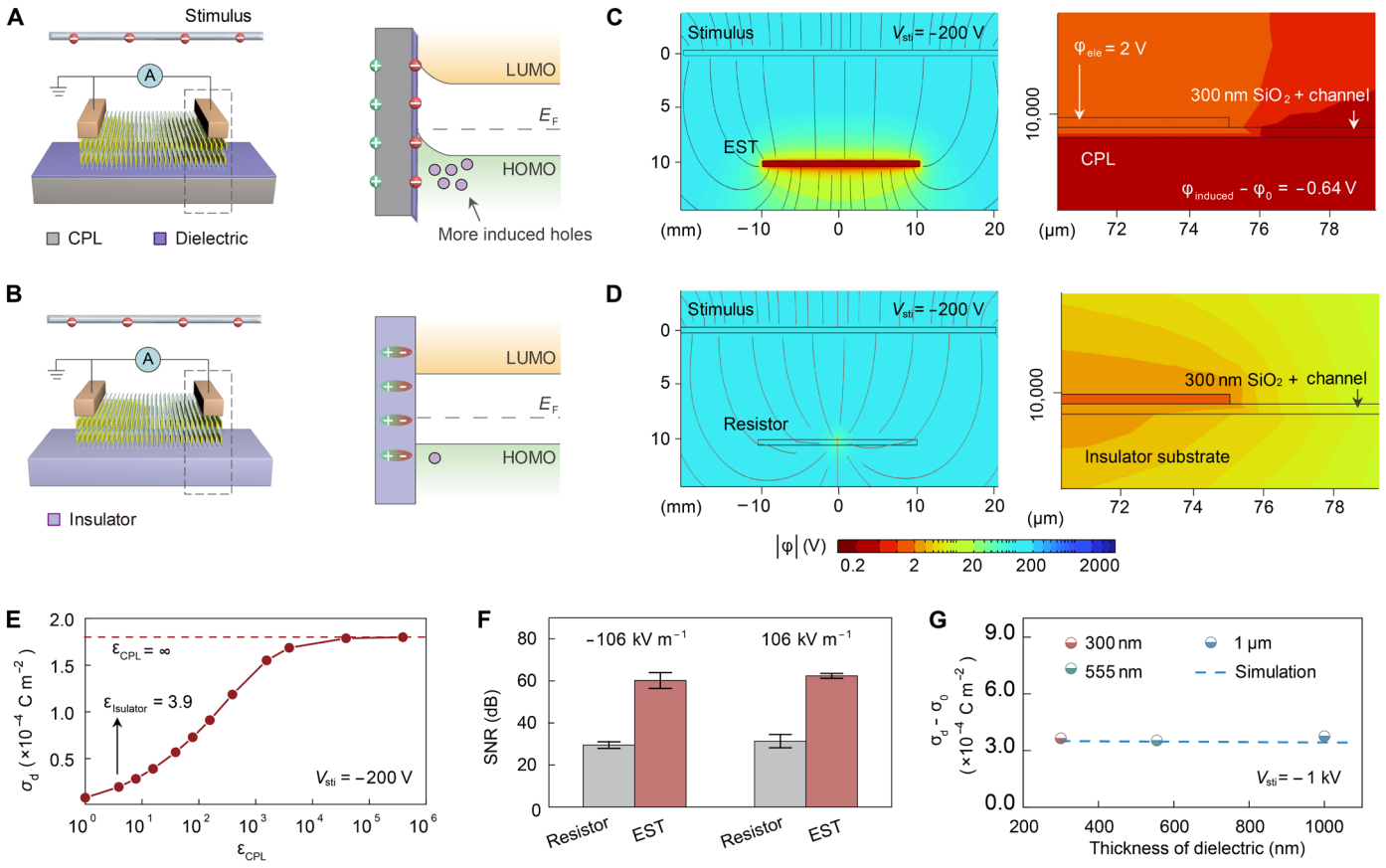

Fig. 2. Charge induction in EST increased by charge-pumping effect. (**A** to **D**) Schematic illustrations [left of (A) and (B)], charge induction mechanism [right of (A) and (B)], and the corresponding simulated potential distribution of devices [(C) and (D)] with OSCFs (yellow) placed on 300-nm SiO_2/CPL (A) and insulator substrate [resistor, (B)] under a negatively voltage–biased stimulus. Field lines terminate at CPL and induced potential ($\varphi_{induced}$) forms equipotential lines. Right panels in (C) and (D): magnified area of dotted squares in (A) and (B) show potential drops in the insulator substrate, whereas constant $\varphi_{induced}$ is seen in conductive CPL. Schematic [right of (A) and (B)] shows that introducing a conducting CPL increases the induced holes in the channel. Simulation is by FEA. The voltage of the stimulus (V_{sti}) is −200 V. Distance between the stimulus and device is 1 cm. φ_0 represents the potential of CPL without stimulus. (**E**) Simulated induced surface charge density (σ_d) of devices with different ε_{CPL} shows that σ_d grows with ε_{CPL} and approaches infinitely to the value where CPL is conductive. (**F**) Signal-to-noise ratio (SNR) of the EST and resistor shows notable improvement of the EST both in negative and positive stimuli. Error bars are SD (n = 7). (**G**) Experimental (circles) and simulation (dotted line) results show that induced surface charge density ($\sigma_d - \sigma_0$) is constant regardless of different dielectric thicknesses. σ_0 represents the initial surface charge density in the absence of stimulus.

sensitive to ambient temperature and humidity (fig. S4). Notably, the prerequisite for the charge-pump effect is that the CPL must be floating (fig. S5). As a result, the signal-to-noise ratio of EST is twice that of the resistor device, reaching more than 60 dB (Fig. 2F, text S2, and figs. S6 and S7).

In addition, we investigated the role of the dielectric layer in EST. The induced surface charge density increment ($\sigma_d - \sigma_0$) is numerically equal to the specific capacitance of the dielectric layer (C_i) multiplied by $\varphi_{induced} - \varphi_0$. Because C_i is the ratio of the dielectric layer permittivity to thickness, it is easy to assume that the permittivity and thickness of the dielectric layer are the main factors affecting surface charge density. Yet, our simulation and experiments demonstrate that induced $\sigma_d - \sigma_0$ almost did not change (<2%) when the thickness of the SiO_2 dielectric layer increased from 300 to 1000 nm (Fig. 2G and fig. S8). This is because $\varphi_{induced}$ increases with dielectric layer thickness (fig. S9). In our model, the effect of the capacitance of the dielectric layer on charge induction is negligible, and thus the possibility of expanding the diversity of dielectric layers, such as other flexible dielectric polymers.

Programming time-dependent response by tuning channel crystallinity

The steady-state response is fundamental to delivering reliable and accurate sensing in practical applications. Inherently, induced charges moving through the delocalized electron states (HOMO) generate induced currents in the channel of the EST. During this process, the induced charges inevitably fall into charge traps, leading to current attenuation. These traps are characterized by a trap density of states (TDOS) with an exponential distribution in the bandgap. We performed technology computer-aided design (TCAD) simulations (see text S3, table S2, and fig. S10) to predict time-dependent response behavior of EST (*29*). The model is calibrated by a transfer curve of a transistor based on OSCFs without grain boundaries (fig. S11). On this basis, a part of the ordered channel is "knocked off" as equivalent grain boundaries throughout the channel, which is independently assigned to the TDOS as following exponential expression (*30*–*32*).

$$g_D(E) = \frac{HD}{kTCD}\exp\left(\frac{E_V - E}{kTCD}\right) \quad (1)$$

where *HD* is the donor trap density (cm^{-3}), *TCD* is the donor trap characteristic temperature (K), *k* is the Boltzmann constant (eV K^{-1}), and $E_V - E$ is the energy difference between trap states and HOMO. The simulated time-dependent response curves for different trap distributions via orthogonally changing the characteristic width of trap states (*k*TCD) and HD are shown in fig. S12. Ignoring the charging process within 0.2 s of an applied electric field, the time-dependent response curve shows an excellent fit with the modified Kohlrausch decay function (stretched exponential relaxation; text S4) (*33*–*35*).

$$I(t)/I_{0,r} = A_0 e^{-(t/\tau)^{\beta}} + I_{\infty}/I_{0,r} \quad (2)$$

where $I(t)$ is time-dependent current, $I_{0,r}$ is initial current, A_0 is prefactor, τ is a time constant, and β is stretching exponent ($0 < \beta \leq 1$) (*36*). Decay index $I_\infty/I_{0,r}$ represents the ratio of the stable response current to the initial current (*37*). The contour map of fitting $I_\infty/I_{0,r}$ shows that $I_\infty/I_{0,r}$ gets larger toward the bottom left corner (Fig. 3A). It demonstrates that the time-dependent response can be programmed by adjusting the trap distributions of semiconductors.

As an experimental verification, we programmed a time-dependent response of the EST with different semiconductor crystallinity. We obtain OSCFs of dioctyl-substituted dibenzo[d,d′]thieno[3,2-b;4,5-b′]-dithiophenes (C_8-DBTDT) by water surface–assisted confined assembly (Fig. 3B). The butterfly shape curve of the crystal's polarizing brightness corresponding to a 360° in-plane rotation further confirms that the sample has long-range order (Fig. 3C and fig. S13). Characterization of the film edge by atomic force microscopy (AFM) revealed that the OSCFs are five-layer thick (15.4 nm; figs. S14 and S15) with a nearly atomically flat surface (mean square roughness, ~0.3 nm). High-resolution AFM shows that the lattice of OSCFs ($a = 4.28$ Å and $b = 10.82$ Å) is consistent with bulk crystals and in-plane arrangements are indexed to the (100) and (010) lattice planes that correspond to a prominent in-plane carrier transport path (Fig. 3D and figs. S16 and S17). Appropriately increasing the width/length ratio of the device is conducive to improving the response ratio (fig. S18). Therefore, the excellent two-dimensional self-assembly capability of C_8-DBTDT drives the growth of large-area single crystals, which is crucial for device optimization (fig. S19). Moreover, hole injection from the contact electrode to C_8-DBTDT thin film is effective because the measured HOMO (−5.25 eV) matches the Fermi level of gold contact (fig. S20).

Then, we also fabricated polycrystalline films, layered thin films (layer-TFs) and island thin films (island-TFs) by spin-coating method, as control samples. AFM images show that samples have distinct grain boundaries, wider height distribution (peak width at half height ~14.3 nm for layer-TFs and ~58.7 nm for island-TFs), and tens of times greater root mean square roughness (~11.3 nm for layer-TFs and ~23.8 nm for island-TFs) than OSCFs (peak width at half height ~0.3 nm and root mean square roughness ~0.3 nm) (Fig. 3E and fig. S21). All three films are configured into the same device configuration with the CPL. With the increase of crystallinity, the device realizes the transition from a quasi-steady state to a steady state response (Fig. 3F and fig. S22), which matches well the simulation (fig. S23). It is also observed that an increased response ratio from island-TFs (1.64 ± 0.72) and layer-TFs (6.34 ± 0.77) to OSCFs (52.22 ± 4.00). Meanwhile, compared with island-TFs, OSCFs with an atom-level flat surface reduce the contact resistance by an order of magnitude (fig. S24 and table S3), resulting in a lower carrier injection barrier. OSCF transistors exhibit negligible hysteresis in the transfer curve regardless of fast or slow sweeping, indicating low trap states and perfect carrier transport interfaces (fig. S25). On the contrary, layer-TFs and island-TFs present obvious sweep speed dependent hysteresis (fig. S26).

The two-dimensional carrier concentration profiles show lower hole concentration at the "knocked off" regions of layer-TF and island-TF channel than that of OSCF channel, indicating increased carrier recombination at the grain boundary (Fig. 3G). Fitting the response curves with the model, the extracted TDOS in the grain boundary region for all three channels show island-TFs have a wider tail distribution from the band edge than layer-TFs and OSCFs (Fig. 3H). $I_\infty/I_{0,r}$ of OSCF channel remains 0.99, which is notably higher than layer-TFs (0.56) and island-TFs (0.11) (Fig. 3I). Decay in our model is strongly coupled to the β value, such that a small β value yields sustained decays. We used $\Delta E_B = E_a/\beta$ to estimate the average barrier height that carriers need to overcome (*38*). E_a, which represents thermal activation energy, is estimated by temperature-dependent conductivity following the Arrhenius relation (Fig. 3J and fig. S27). The average barrier height of devices reduces by nearly one order of magnitude from 393.6 meV (island-TFs) to 46.2 meV (OSCFs). As a result, crystallinity can effectively adjust the time-dependent response of the device and the OSCFs enable the device to have a steady-state response and highly sensitive electric field sensing capability.

EST for impalpable electro-sensing

Our OSCF-based EST device shows a distinctive stepwise response to negative (−0.75 to −345 kV m^{-1}) and positive (4.2 to 106 kV m^{-1}) electric fields, respectively (Fig. 4, A and B). On the contrary, the traditional sensing electrode shows a transient response to the electric field but is not positively correlated with the field strength. The response ratio (78.06 ± 14.17) and sensitivity [0.19 ± 0.01 (kV $m^{-1})^{-1}$] of EST are ~100 times and ~70 times higher than that of resistor devices, respectively. The detection limit of EST is -0.12 ± 0.09 kV m^{-1}, which is 4.15% that of the resistor device (Fig. 4C, fig. S28A, and text S2). Different from the upward stepwise response under a negatively charged stimulus, the device shows a downward stepwise response under a positively charged stimulus (Fig. 4B). This is due to the positive electric field induced positive $\varphi_{induced}$ (fig. S29), causing channel depletion. The detection limit of the EST for a positive electric field is 0.61 ± 0.10 kV m^{-1}, which is 1.84% that of resistor configuration (Fig. 4D and fig. S28B). The power consumption and energy consumption of EST under steady-state conditions and transient conditions in an electrical field of −300 kV m^{-1} are 0.4 μW and 1.1×10^{-7} J (fig. S30), respectively, demonstrating good energy efficiency for practical system integration.

Our device can recognize the approach and withdrawal of charged objects via enhancement (upward response) or suppression (downward response). We used negatively charged polytetrafluoroethylene (PTFE) with a surface potential of -2.0 ± 0.3 kV and positively charged polypropylene (PP) films with a surface potential of 800 ± 160 V as stimulus objects. As a piece of (−) PTFE moves from 365 to 5 mm away from the EST, the current rises from ~5.5 to ~384.2 nA (Fig. 4E, top). Conversely, when the stimulus is replaced with (+) PP, the current decreases from ~5.5 to ~0.5 nA. Carrier regulation in the channel is reversible and instant, with the current returning to its initial state upon removing the charged objects. This also compensates for the limitation of traditional sensing electrodes,

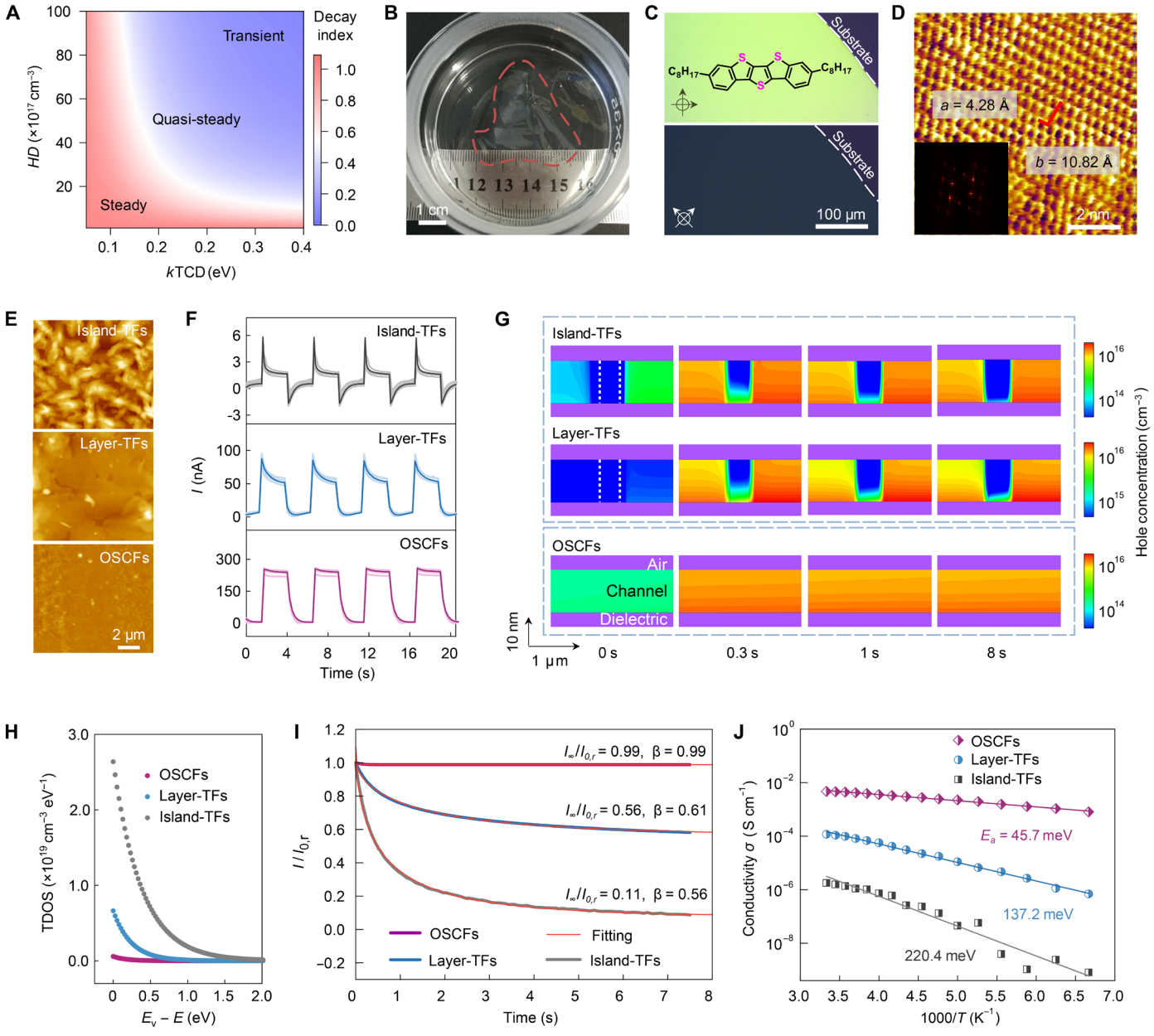

Fig. 3. Crystallinity programs time-dependent response in EST. (**A**) Heatmap of decay index ($I_\infty/I_{0,r}$) with donor trap density (*HD*) and characteristic width (*k*TCD) of trap density of states (TDOS) shows narrowing *k*TCD of TDOS and reducing HD enable the device to transition from a transient to a steady response. (**B**) Optical photograph of C_8-DBTDT OSCFs grown on the water surface. (**C**) Cross-polarized optical micrographs of OSCFs display uniform color change when rotated clockwise from 0° (up) to 45° (bottom). Crossed arrows represent orthogonal polarizers and analyzers. Dash lines indicate film edge. Structural formula is C_8-DBTDT. (**D**) High-resolution AFM and fast Fourier transform image (inset) of OSCFs show periodic patterns that are consistent with lattice parameters in bulk single crystal (a = 4.28 Å, b = 10.82 Å). (**E**) AFM topographic images show OSCFs with lower roughness [root mean square (RMS) ~0.3 nm] and fewer grain boundaries than layered thin films (layer-TFs; RMS ~11.3 nm) and island thin films (island-TFs; RMS ~23.8 nm). (**F**) Corresponding dynamic responses of device based on three samples in periodic spatial electric field stimulus of −300 kV m^{-1} (n = 5). (**G**) Two-dimensional hole concentration profiles of island-TF, layer-TF, and OSCF channel show the hole concentration at grain boundaries decays with time. Region between two white dotted lines represents the equivalent grain boundary of the channel. (**H**) Simulated TDOS at the grain boundary of three samples. (**I**) Time-dependent fitting model shows that increasing the crystallinity enables the device to transition from a transient to a steady response. (**J**) Temperature-dependent conductivity of the three devices indicates the activation energy (E_a derived from the slope of the fitting curve by the Arrhenius-type relation) of OSCF-based EST is much lower than the other two.

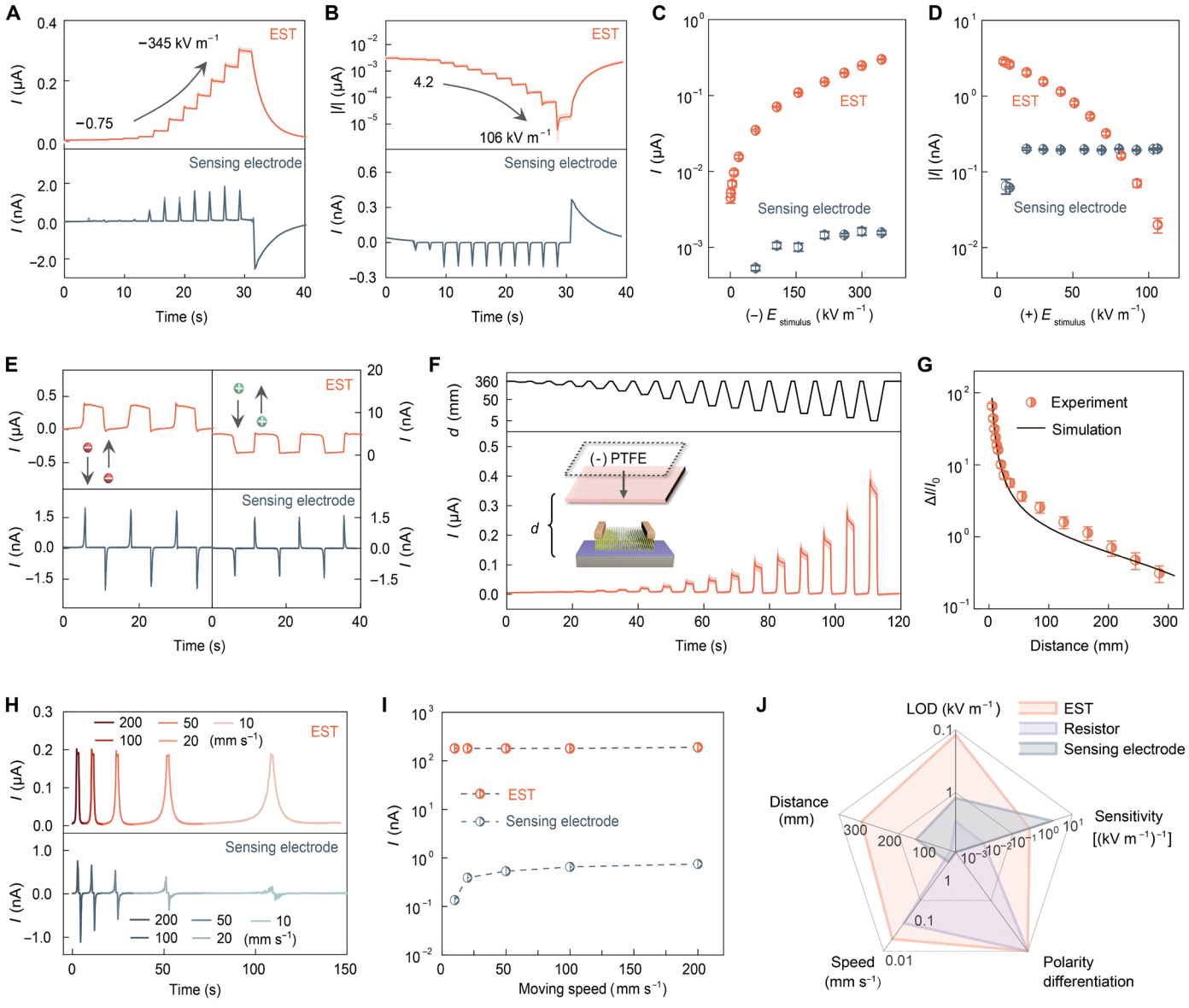

Fig. 4. Impalpable electro-sensing capability of the EST. (**A** to **B**) Dynamic current responses of the EST with stepwise electric field strength. The signal-on (hole accumulation in the channel) and signal-off (hole depletion in the channel) responses of EST are seen for negative (A) and positive electric field (B), respectively. Traditional sensing electrodes can only get a transient response. (**C** and **D**) Response currents with electric field strength show a positive correlation in EST. (**E**) Dynamic current responses of the EST and sensing electrode when stimuli with different polarity approaches from 365 to 5 mm away from the device (arrow down) and leave the same way (arrow up) shows the polarity differentiation ability of EST. Objects moved at 300 mm s^{-1} unless stated otherwise. (**F** and **G**) Current response for negatively charged (−) PTFE at different distances, *d*, (from 325 to 5 mm) to the EST (F) and the relationship between response and distance matched with simulation (G). Error bars are SD ($n = 7$). (−) PTFE, negatively charged polytetrafluoroethylene. (**H**) and (**I**) Response currents of PTFE stimulus moving from 365 to 9 mm at different moving speeds show detectability to slow-moving objects. (**J**) Key performance indicators of EST compared to the resistor-type sensor and the sensing electrode. LOD, limit of detection.

which cannot to distinguish the movement direction of objects with different polarities (Fig. 4E, bottom).

Having a large detection distance is beneficial to give artificial central systems more time to make decisions. As shown in Fig. 4F and fig. S31, the response current of the EST gradually increased as a periodically oscillating (−) PTFE object moved closer (from 325 to 5 mm. The relationship between the response current and object distance is well matched with our device simulation (Fig. 4G), which conforms to the empirical power function, $\Delta I/I_0 = 473.4\ d^{-1.2}$ (fig. S32). The consistent response current at different moving speeds of the object (Fig. 4H) and stable response, while the object held static (fig. S33), indicates that the response is almost unaffected by the moving speed, whereas the response current of the sensing electrode falloff as the object moves slower and is almost undetectable at the speed of 1.71 mm s^{-1} (Fig. 4I). Our EST can detect a moving (−) PTFE object down to 20 μm s^{-1} (fig. S34). High-frequency response proves that the device can detect object vibrations up to 20,000 Hz (fig. S35). The cycle test (fig. S36) and electric field aging test (fig.

S37) show that the device has no observable degradation, which is beneficial to a reliable artificial sensing system. Our EST ultimately is sensitive to impalpable electro-signal with polarity discrimination (Fig. 4J and tables S4 and S5), laying the foundation for an artificial electrosensory system.

An artificial electrosensory system for impalpable electro-navigation and searching behavior

To endow the robot with impalpable perception, we installed our EST on the head of a crawling robot as a receptor to implement an artificial electrosensory system (Fig. 5A). The electromagnetic interference resistance of EST enables it to maintain accuracy when integrated into a robot (fig. S38). Like the electrosensory loop of electrogenic fishes, the EST device detects electric field signals, converts them into digital signals using an analog-to-digital converter, and provides feedback (processed by a micro-controller) to the robot as actionable commands. To mimic how electric fish wiggle their bodies toward a target in response to an electric field (*39*), we created an electrical boundary above the road by suspending in the air a strip of negatively charged PTFE (surface potential is -2.0 ± 0.3 kV) on the left and positively charged PP (surface potential is 800 ± 160 V) on the right side of the road. The robot crawls on the road in the direction of the head below the suspended electrical boundary. The robot turns right when it detects a negative electric field and turns left in response to a positive field. The road is 1.5 m wide, 1.8 m long, and symmetrical along the central axis. The vertical distance between the robot and the electrical boundary is around 17 cm.

Without the electrosensory system, the robot fails to detect the electrical boundary and cannot navigate properly (Fig. 5, B and C). When equipped with an electrosensory system based on layer-TF-based EST, the robot recognizes only the negative boundary on the left side of the road to achieve unilateral navigation (Fig. 5, D and E). With an electrosensory system based on OSCF-based EST, the robot effectively recognized both positive and negative boundaries on the right and left sides of the road to realize bilateral navigation until the end of the road (Fig. 5, F and G, and movie S1). We quantified the navigation of the robot by calculating its swing ratio, the ratio of the lateral maximum position that the robot can reach from the central axis to half-road width. The swing ratio quantified by the trajectories starting at eight different starting angles (20° to 160° with 20° intervals; fig. S39) is plotted for robots without (Fig. 5H) and with a unilateral (Fig. 5I) and bilateral (Fig. 5J) electrosensory system. Only robots with a bilateral electrosensory system can achieve a low swing ratio (all below 0.4) at any starting angle to the end of the road.

Another important function of the bio-electroreceptor is to detect prey hidden in the sand (*40*). Similarly, our electrosensory system can also identify invisible objects with charges. To demonstrate this, we charged a ping-pong ball by friction (surface potential is -600 ± 80 V) and then placed it in an opaque box (Fig. 5K). Here, the EST device is attached to the bottom of the robot and maintains a 5-cm clearance from the box top. When a robot navigates past the box, it successfully locates the target and stomps as a sign (movie S2).

Regardless of where the ping-pong ball is hidden, electrosensory systems based on OSCFs EST detected the ball with high sensitivity (90.0%) and accuracy (96.7%, 30 independent experiments), while systems based on layer-TFs and island-TFs EST displayed feeble feedback signals and poor sensitivity (13.3 and 56.7%, respectively) and accuracy (64.0 and 75.0%, respectively) (Fig. 5L). Besides the ping-pong ball, the electrosensory system based on OSCFs EST could also accurately identify different charged polymer films hidden below a shelter (fig. S40). These results show the electrosensory system can reliably detect hidden objects.

DISCUSSION

We have reported an EST that can emulate the electroreceptive cell to perceive weak spatial electric field with polarity differentiation and established a compact model to reveal the charge dynamics of the device. Unlike conventional transistors, our EST eliminates bias control and incorporates spatial electric field sensing capabilities. The charge-pumping effect of the floating CPL increases the device signal-to-noise ratio markedly, and crystallinity programs the time-dependence response. Under the guidance of the above understanding, we constructed highly sensitive EST devices based on organic semiconductor crystals with a detection limit as low as -0.12 kV m^{-1} in negative stimulus and 0.61 kV m^{-1} in positive electric field. When implemented on a crawling robot, our EST enabled the robot to navigate and detect hidden objects, like electrogenic fishes. The results of this study are expected to advance the design and development of electrosense devices for impalpable perception, which can be used to patrol hazardous environments, operate search-and-rescue missions, and extend the perceptual abilities of artificial systems.

MATERIALS AND METHODS

Growth of OSCFs

A water surface–assisted confined strategy was used to grow the OSCFs. The C_8-DBTDT crude product was purchased from SunaTech Inc. and then purified by column chromatography on silica gel using hexane as eluent to give C_8-DBTDT as a white solid after recrystallization in isopropyl alcohol and removal of solvent in vacuum. ^{1}H NMR (400 MHz, CD_2Cl_2): δ 7.78 to 7.80 (d, $J = 8$ Hz, 2H), 7.72 (s, 2H), 7.30 to 7.32 (d, $J = 8$ Hz, 2H), 2.75 to 2.78 (t, $J = 8$ Hz, 4H), 1.66 to 1.73 (m, 4H), 1.28 to 1.35 (m, 20H), 0.87 to 0.90 (t, $J = 8$ Hz, 6H). The purified product was first dissolved in toluene at a concentration of 1 mg ml^{-1}. The glass bottle (60 ml) was washed three times with deionized water and ultrasonically cleaned with ethanol, and then 50 ml of Milli-Q water (18 megohm·cm) was poured into the bottle to form the calm water surface for crystal growth. Thirty microliters of C_8-DBTDT/toluene solution was injected onto the water surface and then sealed until the solvent completely evaporated. As a result, the OSCFs floating on the water surface were obtained and can be transferred to the substrate of choice for characterization or device integration.

Material characterization

Cross-polarized optical micrographs were obtained using Olympus BX53 polarized optical microscopes on SiO_2 (300 nm)/Si wafer. Noncontact mode AFM was performed using Park NX10 to determine the film thickness and surface topography, and high-resolution AFM was conducted on Asylum Research Cypher S with the qp-BioAC-10 tip under ambient conditions. Powder x-ray diffraction measurements were carried out in Bragg-Brentano focusing geometry on Panalytical XPert Pro at 40 kV and 30 mA with monochromatic Cu Ka radiation to realize an out-of-plane 2θ scan. The ultraviolet-visible near-infrared absorption spectrum of the

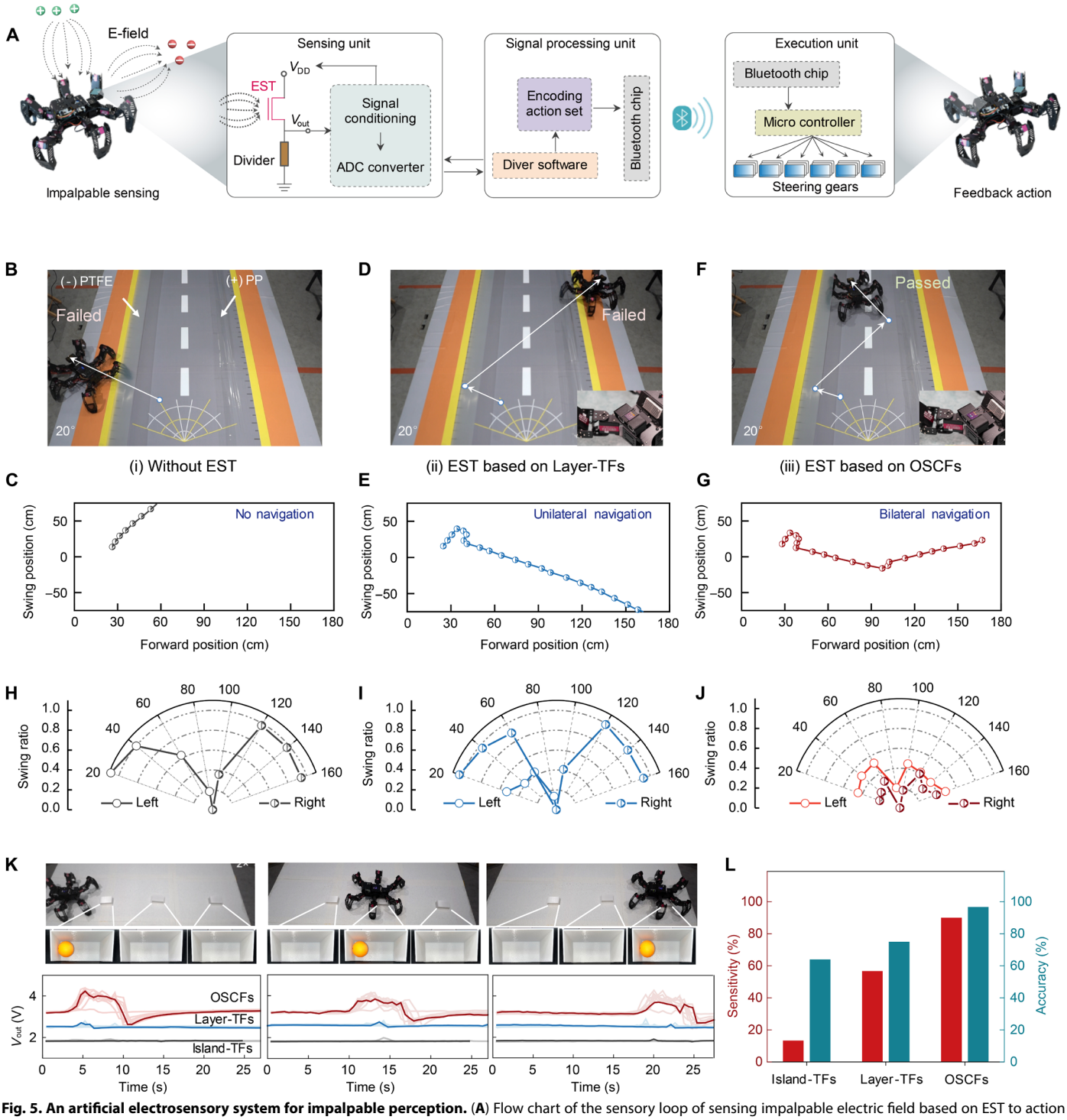

Fig. 5. An artificial electrosensory system for impalpable perception. (**A**) Flow chart of the sensory loop of sensing impalpable electric field based on EST to action feedback. (**B** to **G**) Photographs [(B), (D), and (F)] and the corresponding recorded trajectories [(H), (I), and (J)] of robots without an electrosensory system [(B) and (C)], with a unilateral system based on layer-TFs [(D) and (E)] and a bilateral system based on OSCFs [(F) and (G)]. Only robots with the bilateral system successfully responded to the suspended electrical boundaries and navigated to the end of the road. The dash line indicates the trajectory of the robot. The angle between the starting direction of the robot and the vertical direction of the road is 20°. Inset in (C) and (D): Photographs show artificial electroreceptors mounted on the robot's head. (**H** to **J**) The swing ratio of different starting angles quantifies the effectiveness of robots without (H) and with a unilateral (I) and bilateral (J) electrosensory system. The hollow circle and patterned circle represent the trajectory of the robot crawling on the left and right of the center line, respectively. (**K**) Photographs (top) and the corresponding feedback signals (bottom) for robots with electrosensory systems based on OSCFs, layer-TFs and island-TFs crawling from left to right in search of an orange sphere hidden in an opaque box. Whether the ball is hidden in the first (left panel), second (middle panel), or third box (right panel), only the robot with the OSCF-based EST system displayed distinct feedback signals and correctly located the ball. (**L**) Statistical analysis shows electrosensory systems with OSCFs are sensitive and accurate in perceiving impalpable objects. Sensitivity (red bars) is the ratio of true positive to true positive and false negative. Accuracy (green bars) is the ratio of true positive to all sets.

spin-coating [C_8-DBTDT/chlorobenzene solution (5 mg ml) at 2000 rpm for 60 s] thin film on a quartz substrate was measured with Lambda 950 spectrometer. Ultraviolet photoelectron spectroscopy characterization for the crystal film on an indium tin oxide–coated glass slide was taken with Kratos AXIS Supra with an unfiltered He(I) discharge lamp (21.2 eV) as the excitation source and a 110-μm aperture as the laser collimation. Transmission electron microscopy and selected-area electron diffraction measurements were performed on a JEOL JEM-1011 at an accelerating voltage of 100 kV. The cross section of EST with sharp edges was prepared with the help of a dicing blade without additional surface treatment. The scanning electron microscope was performed on FESEM JEOL JSM-7600F at an accelerating voltage of 2 kV.

Fabrication of EST

The OSCFs were transferred to 2 cm × 2 cm SiO_2 (300 nm)/Si substrate, which was cleaned in sequence with piranha solution and deionized water. After that, 50-nm interdigitated gold contact electrodes by thermal evaporation through a shadow mask. The channel size was 50 μm length × 1.5 mm width. Two polycrystalline film–based devices are referred to as layer-TFs and island-TFs as control samples. C_8-DBTDT/toluene (2 mg ml^{-1}; dissolved in 60°C) and C_8-DBTDT/chloroform (5 mg ml^{-1}; dissolved in 25°C) solutions were spin-coated at a speed of 2000 rpm on preheated SiO_2 (300 nm)/Si at 60°C, respectively. The subsequent contact electrode preparation is the same as above.

Characterization of electrical properties

The electrical properties were measured on a semiconductor analyzer (Keithley 4200-SCS) in an air atmosphere at room temperature. Testing of the device under voltage-biased stimuli is performed in a shielded box. The electric field is generated by a voltage-biased indium tin oxide–coated slide with the size of 4 × 4 cm. Contactless control of different distances is achieved by three-axis movable platform modules with a programmable logic controller. The surface potential of charged objects was in situ calibrated by the electro-field meter (EFM 022, Kleinwächter GmbH). The temperature-dependent conductivity with different electric fields was measured in cryogenic probe stations (Advanced Research Systems Inc.).

FEA simulations

The numerical analysis of the model uses the COMSOL FEA to solve the Poisson equation with boundary value theorem to obtain the induced voltage of the CPL and induced charge injection at the electrode/semiconductor interface. Detailed model analysis and geometrical/material parameters in the simulation are described in text S1.

TCAD simulations

To understand the EST performance, physics-based device simulations were performed using Silvaco TCAD device simulator. The device geometry parameters are set according to the actual device size. Physical models such as Poole-Frenkel mobility model, Shockley-Read-Hall recombination model, and Boltzmann carrier statistics were used to numerically solve the drift-diffusion transport equation and simulate the electrical behavior of EST. Exponential TDOS with a continuous distribution has been used to better represent trap states in disordered organic semiconductors. Additional details for the simulations are provided in the text S3.

Artificial electrosensory system

The system consists of an EST device for sensing, a data acquisition unit (DAQ, NI USB-6251) for capturing the sensing signal, a computer for implementing the signal processing with MATLAB, a wireless data transmission module (HC-05 Bluetooth) for sending control command, and a six-legged crawling robot for executing actions.

Supplementary Materials

The PDF file includes:

Supplementary Text S1 to S5
Figs. S1 to S40
Tables S1 to S5
Legends for movies S1 and S2
References

Other Supplementary Material for this manuscript includes the following:

Movies S1 and S2

REFERENCES AND NOTES

1. S. Qu, L. Sun, S. Zhang, J. Liu, Y. Li, J. Liu, W. Xu, An artificially-intelligent cornea with tactile sensation enables sensory expansion and interaction. *Nat. Commun.* **14**, 7181 (2023).
2. C. Wan, P. Cai, X. Guo, M. Wang, N. Matsuhisa, L. Yang, Z. Lv, Y. Luo, X. J. Loh, X. Chen, An artificial sensory neuron with visual-haptic fusion. *Nat. Commun.* **11**, 4602 (2020).
3. S. Li, X. Chen, X. Li, H. Tian, C. Wang, B. Nie, J. He, J. Shao, Bioinspired robot skin with mechanically gated electron channels for sliding tactile perception. *Sci. Adv.* **8**, eade0720 (2022).
4. M. Wang, Z. Yan, T. Wang, P. Cai, S. Gao, Y. Zeng, C. Wan, H. Wang, L. Pan, J. Yu, S. Pan, K. He, J. Lu, X. Chen, Gesture recognition using a bioinspired learning architecture that integrates visual data with somatosensory data from stretchable sensors. *Nat. Electron.* **3**, 563–570 (2020).
5. S. N. Flesher, J. E. Downey, J. M. Weiss, C. L. Hughes, A. J. Herrera, E. C. Tyler-Kabara, M. L. Boninger, J. L. Collinger, R. A. Gaunt, A brain-computer interface that evokes tactile sensations improves robotic arm control. *Science* **372**, 831–836 (2021).
6. G. Gu, N. Zhang, H. Xu, S. Lin, Y. Yu, G. Chai, L. Ge, H. Yang, Q. Shao, X. Sheng, X. Zhu, X. Zhao, A soft neuroprosthetic hand providing simultaneous myoelectric control and tactile feedback. *Nat. Biomed. Eng.* **7**, 589–598 (2023).
7. A. Chortos, J. Liu, Z. Bao, Pursuing prosthetic electronic skin. *Nat. Mater.* **15**, 937–950 (2016).
8. S. Raspopovic, G. Valle, F. M. Petrini, Sensory feedback for limb prostheses in amputees. *Nat. Mater.* **20**, 925–939 (2021).
9. Y. Huang, J. Zhou, P. Ke, X. Guo, C. K. Yiu, K. Yao, S. Cai, D. Li, Y. Zhou, J. Li, T. H. Wong, Y. Liu, L. Li, Y. Gao, X. Huang, H. Li, J. Li, B. Zhang, Z. Chen, H. Zheng, X. Yang, H. Gao, Z. Zhao, E. Song, H. Wu, Z. Wang, Z. Xie, K. Zhu, X. Yu, A skin-integrated multimodal haptic interface for immersive tactile feedback. *Nat. Electron.* **6**, 1020 (2023).
10. X. Yu, Z. Xie, Y. Yu, J. Lee, A. Vazquez-Guardado, H. Luan, J. Ruban, X. Ning, A. Akhtar, D. Li, B. Ji, Y. Liu, R. Sun, J. Cao, Q. Huo, Y. Zhong, C. Lee, S. Kim, P. Gutruf, C. Zhang, Y. Xue, Q. Guo, A. Chempakasseril, P. Tian, W. Lu, J. Jeong, Y. Yu, J. Cornman, C. Tan, B. Kim, K. Lee, X. Feng, Y. Huang, J. A. Rogers, Skin-integrated wireless haptic interfaces for virtual and augmented reality. *Nature* **575**, 473–479 (2019).
11. J. J. Kim, Y. Wang, H. Wang, S. Lee, T. Yokota, T. Someya, Skin electronics: Next-generation device platform for virtual and augmented reality. *Adv. Funct. Mater.* **31**, 2009602 (2021).
12. Y. Xu, M. Wan, X. Zhang, J. Wu, Y. Chen, Q. Chen, G. Gu, Infrared small target detection based on local contrast-weighted multidirectional derivative. *IEEE Trans. Geosci. Remote Sens.* **61**, 1–16 (2023).
13. A. Dutta, Z. Niu, A. M. Abdullah, N. Tiwari, M. A. S. Biswas, B. Li, F. Lorestani, Y. Jing, H. Cheng, Closely packed stretchable ultrasound array fabricated with surface charge engineering for contactless gesture and materials detection. *Adv. Sci.* **11**, 2303403 (2024).
14. L. Ding, Y. Wang, C. Sun, Q. Shu, T. Hu, S. Xuan, X. Gong, Three-dimensional structured dual-mode flexible sensors for highly sensitive tactile perception and noncontact sensing. *ACS Appl. Mater. Interfaces* **12**, 20955–20964 (2020).
15. P. Makushko, E. S. O. Mata, G. S. C. Bermúdez, M. Hassan, S. Laureti, C. Rinaldi, F. Fagiani, G. Barucca, N. Schmidt, Y. Zabila, T. Kosub, R. Illing, O. Volkov, I. Vladymyrskyi, J. Fassbender, M. Albrecht, G. Varvaro, D. Makarov, Flexible magnetoreceptor with tunable intrinsic logic for on-skin touchless human-machine interfaces. *Adv. Funct. Mater.* **31**, 2101089 (2021).
16. S. Zou, L.-Q. Tao, G. Wang, C. Zhu, Z. Peng, H. Sun, Y. Li, Y. Wei, T.-L. Ren, Humidity-based human–machine interaction system for healthcare applications. *ACS Appl. Mater. Interfaces* **14**, 12606–12616 (2022).

17. J. Li, C. Wang, J. Su, Z. Liu, H. Fan, C. Wang, Y. Li, Y. He, N. Chen, J. Cao, X. Chen, Observing proton–electron mixed conductivity in graphdiyne. *Adv. Mater.* **36**, 2400950 (2024).
18. S. J. England, D. Robert, The ecology of electricity and electroreception. *Biol. Rev.* **97**, 383–413 (2022).
19. B. Chen, M. Wu, S. Fang, Y. Cao, L. Pei, H. Zhong, C. Sun, X. Lin, X. Li, J. Shen, M. Ye, Liquid metal-tailored PEDOT:PSS for noncontact flexible electronics with high spatial resolution. *ACS Nano* **16**, 19305–19318 (2022).
20. Y. Hu, Y. Yan, A wearable electrostatic sensor for human activity monitoring. *IEEE Trans. Instrum. Meas.* **71**, 1–10 (2022).
21. S. Zhu, Y. Li, H. Yelemulati, X. Deng, Y. Li, J. Wang, X. Li, G. Li, P. Gkoupidenis, Y. Tai, An artificial remote tactile device with 3D depth-of-field sensation. *Sci. Adv.* **8**, eabo5314 (2022).
22. W. J. Song, Y. Lee, Y. Jung, Y.-W. Kang, J. Kim, J.-M. Park, Y.-L. Park, H.-Y. Kim, J.-Y. Sun, Soft artificial electroreceptors for noncontact spatial perception. *Sci. Adv.* **7**, eabg9203 (2021).
23. Y. Tang, H. Zhou, X. Sun, N. Diao, J. Wang, B. Zhang, C. Qin, E. Liang, Y. Mao, Triboelectric touch-free screen sensor for noncontact gesture recognizing. *Adv. Funct. Mater.* **30**, 1907893 (2020).
24. Y. Du, P. Shen, H. Liu, Y. Zhang, L. Jia, X. Pu, F. Yang, T. Ren, D. Chu, Z. Wang, D. Wei, Multi-receptor skin with highly sensitive tele-perception somatosensory. *Sci. Adv.* **10**, eadp8681 (2024).
25. W. Liu, Y. Niu, Q. Chen, H. Jiang, F. Xu, G. Zhu, High-performance proximity sensors with nanogroove-template-enhanced extended-gate field-effect transistor configuration. *Adv. Electron. Mater.* **5**, 1900586 (2019).
26. H. Wang, Y. Tong, X. Zhao, Z. Song, Q. Tang, Y. Liu, Ultrasensitive charged object detection based on rubrene crystal sensor. *IEEE Trans. Electron Devices* **66**, 3139–3143 (2019).
27. H. Wang, Q. Tang, X. Zhao, Y. Tong, Y. Liu, Ultrasensitive flexible proximity sensor based on organic crystal for location detection. *ACS Appl. Mater. Interfaces* **10**, 2785–2792 (2018).
28. I. Shoji, H. Wada, K. Uto, Y. Takeda, T. Sugimoto, H. Matsui, Visualizing quasi-static electric fields with flexible and printed organic transistors. *Adv. Mater. Technol.* **6**, 2100723 (2021).
29. F. M. Hossain, J. Nishii, S. Takagi, A. Ohtomo, T. Fukumura, H. Fujioka, H. Ohno, H. Koinuma, M. Kawasaki, Modeling and simulation of polycrystalline ZnO thin-film transistors. *J. Appl. Phys.* **94**, 7768–7777 (2003).
30. J. Werner, M. Peisl, Exponential band tails in polycrystalline semiconductor films. *Phys. Rev. B.* **31**, 6881–6883 (1985).
31. J. Shen, J. Yang, Physical mechanisms in double-carrier trap-charge limited transport processes in organic electroluminescent devices: A numerical study. *J. Appl. Phys.* **83**, 7706–7714 (1998).
32. D. Gupta, N. Jeon, S. Yoo, Modeling the electrical characteristics of TIPS-pentacene thin-film transistors: Effect of contact barrier, field-dependent mobility, and traps. *Org. Electron.* **9**, 1026–1031 (2008).
33. G. Dicker, M. P. de Haas, D. M. de Leeuw, L. D. A. Siebbeles, Origin of the stretched-exponential hole relaxation in regioregular poly(3-hexylthiophene). *Chem. Phys. Lett.* **402**, 370–374 (2005).
34. T. Jung, Modeling of stretched-exponential and stretched-hyperbola time dependence of threshold voltage shift in thin-film transistors. *J. Appl. Phys.* **117**, 144501 (2015).
35. J. C. Phillips, Stretched exponential relaxation in molecular and electronic glasses. *Rep. Prog. Phys.* **59**, 1133–1207 (1996).
36. D. Monroe, Hopping in exponential band tails. *Phys. Rev. Lett.* **54**, 146–149 (1985).
37. A. Lukichev, Physical meaning of the stretched exponential Kohlrausch function. *Phys. Lett. A* **383**, 2983–2987 (2019).
38. F. R. Libsch, J. Kanicki, Bias-stress-induced stretched-exponential time dependence of charge injection and trapping in amorphous thin-film transistors. *Appl. Phys. Lett.* **62**, 1286–1288 (1993).
39. C. D. Hopkins, K.-T. Shieh, J. McBride, W. Don, M. Winslow, A quantitative analysis of passive electrolocation behavior in electric fish. *Brain Behav. Evol.* **50**, 32–44 (2008).
40. L. A. Wilkens, M. H. Hofmann, Behavior of animals with passive, low-frequency electrosensory systems, in *Electroreception*, T. H. Bullock, C. D. Hopkins, A. N. Popper, R. R. Fay, Eds.(Springer New York: New York, NY, 2005), pp. 229–263.
41. W. Shockley, W. T. Read, Statistics of the recombinations of holes and electrons. *Phys. Rev.* **87**, 835–842 (1952).
42. H. Sirringhaus, Reliability of organic field-effect transistors. *Adv. Mater.* **21**, 3859–3873 (2009).
43. S. G. J. Mathijssen, M. Cölle, H. Gomes, E. C. P. Smits, B. de Boer, I. McCulloch, P. A. Bobbert, D. M. de Leeuw, Dynamics of threshold voltage shifts in organic and amorphous silicon field-effect transistors. *Adv. Mater.* **19**, 2785–2789 (2007).
44. H. H. Choi, M. S. Kang, M. Kim, H. Kim, J. H. Cho, K. Cho, Decoupling the bias-stress-induced charge trapping in semiconductors and gate-dielectrics of organic transistors using a double stretched-exponential formula. *Adv. Funct. Mater.* **23**, 690–696 (2013).
45. T. Yang, Q. Wu, F. Dai, K. Huang, H. Xu, C. Liu, C. Chen, S. Hu, X. Liang, X. Liu, Y.-Y. Noh, C. Liu, Understanding, optimizing, and utilizing nonideal transistors based on organic or organic hybrid semiconductors. *Adv. Funct. Mater.* **30**, 1903889 (2020).
46. R. A. Street, J. E. Northrup, A. Salleo, Transport in polycrystalline polymer thin-film transistors. *Phys. Rev. B.* **71**, 165202 (2005).
47. W.-T. Park, G. Kim, C. Yang, C. Liu, Y.-Y. Noh, Effect of donor molecular structure and gate dielectric on charge-transporting characteristics for isoindigo-based donor–acceptor conjugated polymers. *Adv. Funct. Mater.* **26**, 4695–4703 (2016).
48. V. Rodin, F. Symalla, V. Meded, P. Friederich, D. Danilov, A. Poschlad, G. Nelles, F. von Wrochem, W. Wenzel, Generalized effective-medium model for the carrier mobility in amorphous organic semiconductors. *Phys. Rev. B.* **91**, 155203 (2015).
49. J. Pruefer, J. Leise, J. W. Borchert, H. Klauk, G. Darbandy, A. Nikolaou, B. Iñíguez, T. Gneiting, A. Kloes, Modeling the short-channel effects in coplanar organic thin-film transistors. *IEEE Trans. Electron Devices* **69**, 1099–1106 (2022).
50. Z. H. Guo, H. L. Wang, J. Shao, Y. Shao, L. Jia, L. Li, X. Pu, Z. L. Wang, Bioinspired soft electroreceptors for artificial precontact somatosensation. *Sci. Adv.* **8**, eabo5201 (2022).
51. W. Liu, Y. Duo, J. Liu, F. Yuan, L. Li, L. Li, G. Wang, B. Chen, S. Wang, H. Yang, Y. Liu, Y. Mo, Y. Wang, B. Fang, F. Sun, X. Ding, C. Zhang, L. Wen, Touchless interactive teaching of soft robots through flexible bimodal sensory interfaces. *Nat. Commun.* **13**, 5030 (2022).
52. H. Guo, X. Jia, L. Liu, X. Cao, N. Wang, Z. L. Wang, Freestanding triboelectric nanogenerator enables noncontact motion-tracking and positioning. *ACS Nano* **12**, 3461–3467 (2018).
53. G. Lv, H. Wang, Y. Tong, L. Dong, X. Zhao, P. Zhao, Q. Tang, Y. Liu, Flexible, conformable organic semiconductor proximity sensor array for electronic skin. *Adv. Mater. Interfaces* **7**, 2000306 (2020).
54. F. Xue, L. Chen, L. Wang, Y. Pang, J. Chen, C. Zhang, Z. L. Wang, MoS2 tribotronic transistor for smart tactile switch. *Adv. Funct. Mater.* **26**, 2104–2109 (2016).

Acknowledgments: We thank A. L. Chun for critically reading and editing the manuscript. **Funding:** The project is supported by the National Research Foundation (NRF), Prime Minister's Office, Singapore, under its Campus of Research Excellence and Technological Enterprise (CREATE) program, the Smart Grippers for Soft Robotics (SGSR) program, and Singapore Hybrid-Integrated Next-Generation μ-Electronics (SHINE) Centre, and the Agency for Science, Technology and Research (A*STAR) under its MTC Programmatic Funding Scheme (project no. M23L8b0049, M24M9b0013) Scent Digitalization and Computation (SDC) program and BLISS: Beyond Liquids with In-Situ Solid-state Surficial Sensorics to X.C. **Author contributions:** Conceptualization: X.C., W.H., L.P., Y.L., Cong Wang, and J.L. Methodology: X.C., W.H., C.W., L.L., F.Z., Y.H., Changxian Wang, J.L., Z.L., and X.L. Investigation: X.C., M.W., M.C., Cong Wang, J.L., J.B., X.L., and W.L. Visualization: X.C., W.H., J.L., J.B., X.L. Software: M.W., Cong Wang, N.C., Changxian Wang, Z.L., X.L., and W.L. Writing (original draft): X.C., W.H., Y.L., Cong Wang, Z.L., and X.L. Writing (review and editing): X.C., W.H., C.W., Y.L., N.C., F.Z., Changxian Wang, J.L., Z.L., J.B., X.L., and W.L. **Competing interests:** The authors declare that they have no competing interests. **Data and materials availability:** All data needed to evaluate the conclusions in the paper are present in the paper and/or the Supplementary Materials. The data are available on Dryad https://doi.org/10.5061/dryad.dz08kps7k.

Submitted 17 September 2024
Accepted 12 February 2025
Published 19 March 2025
10.1126/sciadv.ads7457